JM PAPERS

Complex transition pathways in boiling and cavitation

Mirko Gallo[1] , **Filippo Occhioni[1], Francesco Magaletti[1] and Carlo Massimo Casciola[1]**

[1]Department of Mechanical and Aerospace Engineering, Sapienza University of Rome, via Eudossiana 18, Rome 00184, Italy

Corresponding author: Mirko Gallo, mirko.gallo@uniroma1.it

This work combines Navier–Stokes–Korteweg dynamics and rare event techniques to investigate the transition pathways and times of vapour bubble nucleation in metastable liquids under homogeneous and heterogeneous conditions. The nucleation pathways deviate from classical theory, showing that bubble volume alone is an inadequate reaction coordinate. The nucleation mechanism is driven by long-wavelength fluctuations with densities slightly different from the metastable liquid. We propose a new strategy to evaluate the typical nucleation times by inferring the diffusion coefficients from hydrodynamics. The methodology is validated against state-of-the-art nucleation theories in homogeneous conditions, revealing non-trivial, significant effects of surface wettability on heterogeneous nucleation. Notably, homogeneous nucleation is detected at moderate hydrophilic wettabilities despite the presence of a wall, an effect not captured by classical theories but consistent with atomistic simulations. Hydrophobic surfaces, instead, anticipate the spinodal. The proposed approach is fairly general and, despite the paper discussing results for a prototypical fluid, it can be easily extended, also in complex geometries, to any real fluid provided the equation of state is available, paving the way to model complex nucleation problems in real systems.

Key words: drops and bubbles, boiling, cavitation

1. Introduction

The formation of vapour bubbles in a liquid is ubiquitous in natural phenomena. Fascinating examples are the spore release mechanism in the fern *sporangium* annulus (Noblin *et al.* 2012; Montagna *et al.* 2023), the hunting tactic adopted by the snapping shrimp (Versluis *et al.* 2000) and the loss of sap transport capacity due to xylem cavitation

M. Gallo, F. Occhioni, F. Magaletti and C.M. Casciola

(Cochard 2006). Bubble nucleation is also central to several technological applications. Cavitation damage has been a critical issue for decades (Silberrad 1912; Reuter, Deiter & Ohl 2022; Abbondanza *et al.* 2023a, 2024), while boiling is now actively exploited as an efficient mechanism of heat removal for thermal management applications (Bakir & Meindl 2008; Fan & Duan 2020; Zhang *et al.* 2023; Chakraborty *et al.* 2024). Cavitation and boiling are the two sides of the same coin: bubble formation is achieved equivalently by reducing the pressure below the saturation pressure at a given temperature, $p_{sat}(T)$, or by increasing the temperature above the evaporation point at a given pressure, $T_{sat}(p)$. Exceeding these threshold levels does not guarantee the bubble's appearance. The liquid can indeed be held in metastable equilibrium in stretched ($p < p_{sat}$) or superheated ($T > T_{sat}$) conditions without any phase change (Debenedetti 1996; Azouzi *et al.* 2013; Magaletti, Gallo & Casciola 2021). The origin of the metastability can be traced back to a finite free energy barrier between the liquid and the vapour states that renders the liquid–vapour phase change an activated process, where thermal fluctuations are the activating mechanism. This means that a nucleation event always occurs in metastable conditions after waiting a sufficiently long time. However, the time to be awaited exponentially grows with the energy barrier, resulting in an unlikely occurrence, a so-called rare event, except for conditions characterised by small barriers. The thermodynamic limit of metastability is reached at spinodal conditions where the spinodal decomposition, a barrierless phase transition mechanism, occurs. The quantitative prediction of vapour bubble formation in liquids, and phase transition in general, is a long-lasting problem of fluid dynamics and statistical physics, see for example (Lutsko 2017) for an enlightening nucleation résumé. The practical nucleation limit, expressed through the cavitation pressure (Menzl *et al.* 2016), p_{cav}, or the superheat at boiling onset (Gallo *et al.* 2023), $\Delta T_{ons} = T_{ons} - T_{sat}$, precedes the spinodal threshold. However, determining the actual nucleation limit remains challenging. For instance, the cavitation pressure of water has been widely debated due to significant discrepancies between measurement techniques (Caupin & Herbert 2006), with reported values ranging from -30 MPa to -120 MPa at ambient temperature. These discrepancies are largely attributed to sample purity (Lohse & Prosperetti 2016) and difficulty achieving homogeneous nucleation under laboratory conditions (Caupin & Herbert 2006). Lower measured cavitation pressures are considered more representative, as they likely correspond to purer samples. Specifically, since nucleation is an activated process, the cavitation pressure is defined as the pressure at which there is a 50 % probability of observing a bubble, given the experimental sample volume V_{exp} and observation time window τ_{exp} (Azouzi *et al.* 2013). The same arguments apply to the superheat limit, where extremely high measured superheats $T_{ons} \sim 302$ °C (Skripov 1970) stand in stark contrast to boiling temperature measurements showing only a few degrees of superheat (Theofanous *et al.* 2002). Nucleation at solid surfaces introduces further complexity and an even stronger discrepancy in data due to the difficult control in the experimental measurements of dissolved gas content, surface roughness and chemical impurities (Frenkel 1955).

Understanding the fluid dynamics of multiphase systems – and ultimately reconciling them with experimental observations – requires a deep grasp of nucleation and the incipient stages of phase change (Vincent & Marmottant 2017; Gao, Wu & Wang 2021; Yatsyshin & Kalliadasis 2021; Alamé & Mahesh 2024; Chen *et al.* 2025). Nucleation is a key process in multiphase fluid dynamics, driving phase transitions such as bubble and droplet formation. However, its highly uncertain triggering conditions limit the predictive power of current models. Accurately capturing nucleation is therefore essential for developing realistic, multiscale simulations that move beyond empirical assumptions and better represent the complexity of multiphase behaviour.

The reference theory is the classical nucleation theory (CNT) (Blander & Katz 1975), which allows the estimation of the energy barrier, critical cluster dimension and nucleation rate. Despite its physically grounded description of the phenomenon, the estimates for the nucleation rates obtained from CNT differ by orders of magnitude from experiments (Caupin & Herbert 2006; Menzl *et al.* 2016). More sophisticated theories like different extensions of CNT (Lutsko & Durán-Olivencia 2015; Menzl *et al.* 2016), density functional theory (DFT) (Oxtoby & Evans 1988; Talanquer & Oxtoby 1996; Lutsko 2008; Baidakov 2016; Yatsyshin & Kalliadasis 2021) and molecular dynamics (MD) simulations (Allen *et al.* 2009; Diemand *et al.* 2014) can provide better barrier and nucleation rate estimates to correct some of the CNT mispredictions. A common viewpoint in these approaches is considering a multiparameter description of the nucleation process by enriching the list of reactive coordinates with thermodynamic cluster properties (Duran-Olivencia *et al.* 2018).

Here, we propose a mesoscale strategy that clarifies the onset of phase transitions and can be directly coupled one-to-one with hydrodynamic equations, bridging microscopic physics and macroscopic fluid dynamics. By combining Navier–Stokes–Korteweg (NSK) dynamics with rare event techniques, we offer new insights into nucleation pathways and transition times of vapour bubbles in metastable liquids under both homogeneous and heterogeneous conditions.

The nucleation pathways are found to be significantly different from those predicted by CNT, demonstrating that the bubble volume is an inadequate reaction coordinate. The nucleation mechanism arises from long-wavelength fluctuations at large radii, with densities only slightly different from the metastable liquid. The comparison with spherically averaged fluctuating hydrodynamic (FH) simulations of the homogeneous nucleation process, as proposed by these authors in Gallo *et al.* 2020, supports this evidence. For the liquid/vapour thermodynamics, we exploit an approximate DFT approach, specifically, the van der Waals' square gradient model for capillary fluids, also known as the diffuse interface (DI) model (Anderson, McFadden & Wheeler 1998; Lutsko 2011). The string method (E *et al.* 2002) is used to obtain the minimum energy path (MEP), which, in a system with simple gradient dynamics, is associated with the most likely transition path (MLP). Once the MEP has been estimated, we developed a simplified dynamical model that describes the thermodynamic system as a Brownian walker within a metastable basin. This approach allows us to analyse the system's stochastic evolution in the presence of thermal fluctuations. Using Kramers' theory, we then estimated the typical transition frequencies associated with bubble formation. In this framework, the formation of bubbles is interpreted as a rare event driven by noise-induced transitions across an energy barrier. Furthermore, within this metastable landscape, we estimated the effective diffusion of the bubble, which characterises how the bubble's state fluctuates due to stochastic forces. The effective diffusion coefficient is estimated from hydrodynamics, providing a quantitative measure of the bubble's mobility before it undergoes a phase transition. The approach we propose bears some resemblance to previous proposals (Menzl *et al.* 2016), but differs under several substantial respects. In our case, we extract the free energy profile from the MEP of a more realistic model of the liquid–vapour interfacial properties, accounting for the finite thickness of the interface and the intrinsic dependence of surface tension on bubble size, properties which are crucial given the breakdown of the sharp interface assumption at the scale of the nucleating embryo. Hence, the Brownian walker evolves over the appropriate landscape. Moreover, we managed to extract the friction coefficient from the appropriate NSK dynamics. The advantages are that the only input parameters needed by the model are experimentally measurable physical quantities, like planar surface tension and transport coefficients, and the model is naturally suited to deal with heterogeneous conditions and complex geometries.

In the present paper, the homogeneous case is also used as a validation of the proposed approach against state-of-the-art nucleation theories (Menzl *et al.* 2016). Applying this methodology to heterogeneous nucleation reveals distinct effects of surface wettability, particularly under low energy barrier conditions. For moderately hydrophilic surfaces, homogeneous nucleation occurs despite the presence of a wall, an effect overlooked by classical theories but supported by atomistic simulations (Zou, Gupta & Maroo 2018; Sullivan, Dockar & Pillai 2025) since the surface is unable to significantly reduce the nucleation barrier compared with the bulk. In contrast, hydrophobic surfaces anticipate the spinodal limit (Talanquer & Oxtoby 1996), triggering an earlier onset of nucleation via spinodal-like mechanisms. These results demonstrate how surface wettability can fundamentally influence nucleation pathways, with important implications for controlling phase transitions in confined or engineered systems.

2. Results

The two-phase system in the isothermal condition is described here by following the DI approach through the (Landau) free energy functional

$$\Omega\left[\rho\right] = \int_V \left[f_b\left(\rho\right) + f_c\left(\nabla\rho\right) - \mu_{eq}\rho\right] \mathrm{d}V + \oint_{\partial V} f_w\left(\rho\right) \mathrm{d}S, \qquad (2.1)$$

where the van der Waals' square gradient approximation is used to express the non-local excess free energy contribution as $f_c = (\lambda/2)|\nabla\rho|^2$, while f_b is the classical Helmholtz bulk free energy density and μ_{eq} the equilibrium chemical potential, see the Supplementary materials for additional information is available at https://doi.org/10.1017/jfm.2025.10591. The capillary coefficient λ controls the liquid–vapour interface properties, namely the surface tension and the interface thickness. The temperature dependence of all the terms has been neglected for the ease of notation. Finally, the surface contribution f_w arises as a mean field approximation of the fluid–wall interactions and accounts for the wetting properties of the surface. Its explicit expression, derived in Gallo, Magaletti & Casciola 2021,

$$f_w(\rho) = f_w\left(\rho_V\right) - \cos\theta \int_{\rho_V}^{\rho} \sqrt{2\lambda\left[w_b\left(\tilde{\rho}\right) - w_b\left(\rho_V\right)\right]} \mathrm{d}\tilde{\rho}, \qquad (2.2)$$

has been shown to recover the well-known Young condition for the equilibrium contact angle, θ. In the previous expression, $f_w(\rho_V) = \gamma_{SV}$ is the surface energy at the solid–vapour interface, ρ_V is the vapour density and $w_b = f_b - \mu_{sat}\rho$, with μ_{sat} the chemical potential at the saturation condition ($\mu = \partial f_b/\partial\rho$). The starting point for deriving the form of the wall free energy is based on geometric considerations regarding the orientation of the interface normal, aligned with the density gradient, and its contact with the solid surface, along with the expression for surface tension from DI theory, see Gallo *et al.* 2021 for details. In this work, the modified Benedict–Webb–Rubin equation of state (Johnson, Zollweg & Gubbins 1993), mimicking the behaviour of a Lennard-Jones fluid, has been used as $f_b(\rho)$. Here $f_b(\rho)$ is rendered dimensionless using the reference energy $f_{bref} = \epsilon/\sigma^3$ where $\sigma = 3.4 \times 10^{-10}$ m, $\epsilon = 1.65 \times 10^{-21}$ J. The density field is non-dimensionalised with the reference density, $\rho_{ref} = m/\sigma^3$, with $m = 6.63 \times 10^{-26}$ kg. The capillary coefficient is set to $\lambda = 5.224$ with its reference value $\lambda_{ref} = \sigma^5\epsilon/m^2$ ensuring consistency with surface tension values derived from Monte Carlo simulations (Gallo, Magaletti & Casciola 2018; Magaletti *et al.* 2022).

The minimisation of (2.1) leads to the following Euler–Lagrange equation:

$$\frac{\delta\Omega}{\delta\rho} = \mu - \lambda\nabla^2\rho - \mu_{eq} = 0\,, \tag{2.3}$$

expressing the chemical equilibrium in terms of a constant (generalised) chemical potential. This equilibrium condition is supplemented with the boundary condition $\partial f_w/\partial\rho + \lambda\partial\rho/\partial n = 0$ at the solid surface. When the prescribed equilibrium chemical potential corresponds to a metastable condition, $\mu_{spin} < \mu_{eq} < \mu_{sat}$, (2.3) has three solutions: (i) the homogeneous liquid $\rho(\boldsymbol{x}) = \rho_L$; (ii) the homogeneous vapour $\rho(\boldsymbol{x}, t) = \rho_V$; (iii) a two-phase solution with a bubble of a given radius surrounded by the metastable liquid, the critical nucleus representing the transition (or critical) state, i.e. the density configuration $\rho_{crit}(\boldsymbol{x})$ that must be reached to trigger the complete transition from the metastable liquid to the more stable vapour state. Several previous studies have addressed nucleation within frameworks similar to the one employed in the present work (Talanquer & Oxtoby 1996; Baidakov 2016). However, these approaches have been limited to the calculation of critical nucleus profiles and the subsequent estimation of nucleation rates, without resolving the full transition pathway using a rare-event technique. We address here the problem of evaluating the non-trivial solution of case (iii) by exploiting the powerful string method (E *et al.* 2007; Magaletti *et al.* 2021), with the twofold objective of determining both the density field of the critical nucleus and the complete MEP, which describes the system configurations $\rho(s, \boldsymbol{x})$ along a suitable reaction coordinate s advancing through the transition. As detailed in Appendix B, the MEP corresponds to the MLP for a gradient dynamics and thus provides a physically grounded description of the liquid–vapour phase transition. This path can be visualised as a curve (the string), parametrised with s, in the infinite configurational space of the density fields, with the configuration of maximum energy along the MEP representing the transition state. For the homogeneous case, the bubble radius, in each string image along the path, is extracted *a posteriori* from the density field. In the spherical case, a natural radius definition is

$$R(s) = \int_0^\infty r(\partial\rho(r, s)/\partial r)^2\, \mathrm{d}r \Big/ \int_0^\infty (\partial\rho(r, s)/\partial r)^2\, \mathrm{d}r\,, \tag{2.4}$$

which, as will be discussed below, provides a good indicator for the bubble radius converging to the classical one used in sharp interface models. In classical theories, the bubble radius (or its volume, equivalently) is used as the reaction coordinate to describe the progress of the nucleation process, both in homogeneous and heterogeneous conditions. Here CNT is often used to quantitatively depict the energy landscape of the system in terms of the bubble size, with the energy maximum representing the barrier for nucleation and its corresponding critical radius. In figure 1(*a*), the landscapes are plotted in terms of the normalised grand potential $\Delta\Omega/(k_B T) = (\Omega[\rho] - \Omega[\rho_L])/(k_B T)$ as a function of the bubble radius R. Both homogeneous and heterogeneous CNT predictions, at non-dimensional temperature $T = 1.2$ ($T \simeq 1.31$ being the critical temperature) and metastability level $\mu_{lev} = (\mu_{eq} - \mu_{sat})/(\mu_{spin} - \mu_{sat}) = 0.2$, are compared with those obtained by applying the string method to the DI modelling of the two-phase system, as previously described. For $T = 1.2$, we have $\mu_{sat} = -3.9506$, $\mu_{spin} = -4.0491$, $\rho_{Lsat} = 0.5669$ and $\rho_{Lspin} = 0.4798$. The heterogeneous landscape in the plot refers to the specific case of a neutrally wetting surface ($\theta = 90^o$). Despite the low metastability level – corresponding to a condition close to saturation – the discrepancy between the different energy barrier predictions is apparent in both cases, with a difference of the order of 6 %, in line with the results in Shen & Debenedetti 2001. The differences in the nucleation barrier
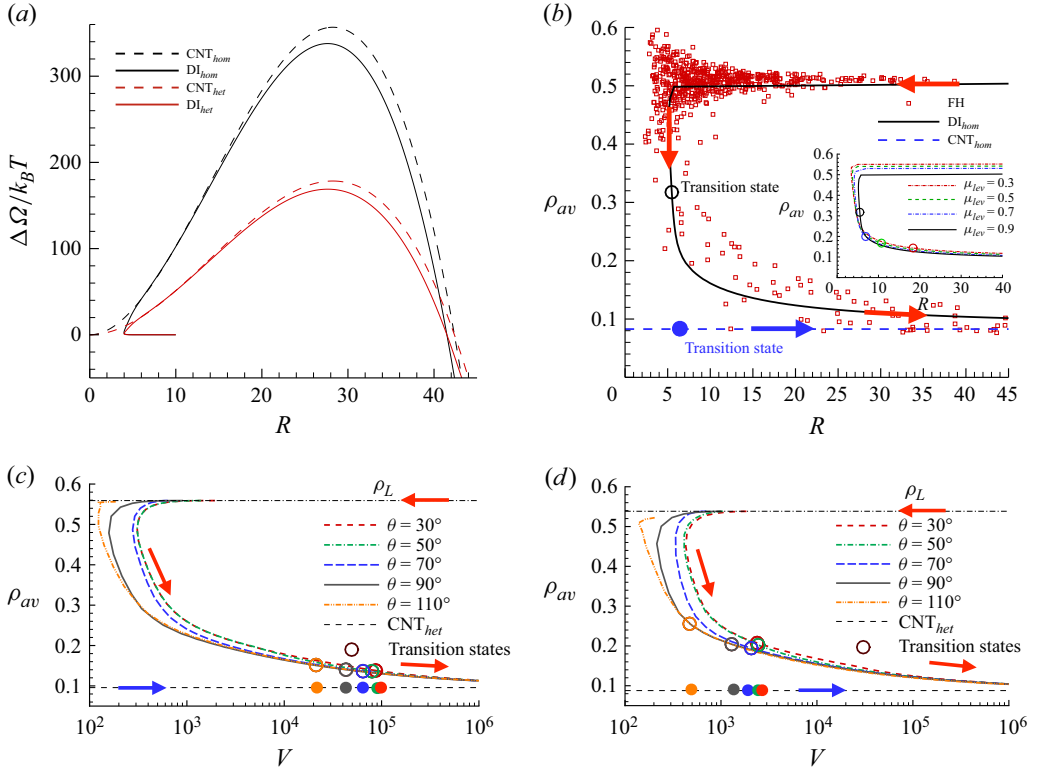
M. Gallo, F. Occhioni, F. Magaletti and C.M. Casciola

Figure 1. (*a*) Comparison of energy landscapes for homogeneous and heterogeneous bubble nucleation predicted by CNT (dashed lines) and DI model (solid lines). The heterogeneous case corresponds to a neutrally wetting surface ($\theta = 90°$). All curves are computed at $T = 1.2$ and $\mu_{lev} = 0.2$. (*b*) Transition path of homogeneous nucleation projected onto the two-coordinate space $\{\rho_{av}, R\}$ at $T = 1.2$, $\mu_{lev} = 0.9$, Arrows identify the phase change direction, red DI and blue CNT, respectively. Transition states from CNT and DI models are marked with full and empty circles, respectively. Red squares indicate ρ_{av} and R during a FH simulation. Inset: transition paths at varying metastabilities, with circles marking the corresponding transition states. The MEPs of heterogeneous nucleation in $\{\rho_{av}, V\}$ space for different surface wettabilities: (*c*) $T = 1.2$, $\mu_{lev} = 0.2$; (*d*) $T = 1.2$, $\mu_{lev} = 0.6$.

are minor, and the critical radii are accurate when approaching saturation conditions. However, discrepancies in the barrier become significantly more pronounced near the spinodal, where CNT predicts a finite barrier, whereas it should vanish. This aspect will be discussed in detail later in the paper. The major difference, however, is the behaviour at low energies where the DI model predicts a non-bijective correspondence between the radius and the energy, suggesting that the radius alone is insufficient to fully describe the nucleation process.

New insights on the transition pathway are gained when the homogeneous nucleation MEP is plotted using a two-coordinate system, $\{\rho_{av}, R\}$, with the average density inside the bubble *a posteriori* evaluated along the string as $\rho_{av} = 3/(4\pi R^3) \int_0^R \rho(r) 4\pi r^2 \, dr$, see figure 1(*b*). The DI model reveals a non-classical C-shape nucleation pathway. In line with the findings on crystal nucleation (Lutsko 2019; Lutsko & Lam 2020), the process starts with a spatially extended density variation of small intensity, hence characterised by a large radius and $\rho_{av} \simeq \rho_L$. Successively, the embryo spatially localises, and its density variation increases. After the transition state is reached, the bubble further grows and

expands, see the red arrows indicating the direction of the transition. The characteristic C-shaped form of the transition pathway is not sensitive to the specific definition of the radius and can also be observed when using the equimolar radius, as shown in the Supplementary materials. The position of the transition state along the curve strongly depends on the degree of metastability μ_{lev}, as shown in the inset in figure 1(*b*): a large and low-density critical embryo characterises conditions close to saturation (small μ_{lev}), in agreement with CNT; when approaching spinodal conditions the critical embryo is instead characterised by small size and a high average density. The C-shape pathway is also confirmed by dynamic simulations with the spherically averaged FH model proposed by these authors in Gallo *et al.* 2020, see Appendix A for details. Due to thermal fluctuations, the system explores a pseudotube in the $\{\rho_{av}, R\}$ space around the zero-temperature MEP provided by the string method. Fluctuations of the average density intensify as the vapour embryo localises in a small region and, consequently, triggers the formation of a low-density cluster that successively expands beyond the transition state. Please note that fluctuations increase when reducing the average (bubble) volume (Gallo 2022). We observe that the MEP is perfectly followed by brute force FH simulations, as demonstrated in figure 1(*b*). This shows unequivocally that, among all the possible thermally induced fluctuations (always present also in stable liquids), the relevant ones for triggering the transition from the metastable liquid state are indeed those predicted by the MEP we have calculated. In addition, despite the nucleation path in FH being expected to differ from the MEP (Grafke, Grauer & Schäfer 2015; Yao & Ren 2022), the bubble nucleation mechanism appears to be well described by free-energy calculations.

Heterogeneous nucleation follows a similar pathway (with the volume *V* instead of the radius) with a small but spatially extended density variation as a precursor of the actual bubble formation. Results at different wettabilities and degrees of metastability are plotted in figure 1(*c,d*). As expected, the volume of the critical nuclei decreases as the contact angle increases, namely, hydrophilic surfaces require a larger critical bubble to initiate the phase transition compared with hydrophobic walls. In addition, the critical volume decreases when the metastability level is increased.

In the case of homogeneous nucleation, figure 2(*a*) reports the nucleation barrier normalised by $k_B T$ as a function of the degree of metastability. As shown, CNT captures well the qualitative trend of the barrier with increasing metastability. However, as the system approaches the spinodal limit, $\mu_{lev} \to 1$, CNT predicts a large limit barrier of approximately $\Delta\Omega_{CNT}^{\star} \simeq 18 k_B T$, whereas the DI approach yields the expected vanishing barrier $\Delta\Omega_{DI}^{\star} \simeq 0$. This discrepancy arises from the gradual breakdown of the sharp interface assumption as the liquid–vapour interfacial thickness becomes comparable to the typical bubble radius. This effect is illustrated in the inset of figure 2(*a*) (red curve right-hand axis), which shows the ratio of the bubble radius to the interface thickness l_{10-90}, defined as the width of the region over which the density transitions from $\rho_{10} = 0.1\rho_L + 0.9\rho_V$ to $\rho_{90} = 0.9\rho_L + 0.1\rho_V$ (Caupin 2005). On the right-hand axis, CNT (dashed line) and DI (solid line) radii are depicted. The DI predicts a non-monotonic behaviour of the critical radius as the spinodal is approached, in contrast to the monotonic trend obtained from CNT. Nevertheless, the actual values of the critical radii remain in reasonably good agreement over the range of metastabilities considered. Figure 2(*b*) shows the transition pathway for homogeneous nucleation in terms of the density profiles $\rho(r)$ along the reaction coordinate *s* of the string. Precritical profiles are shown in blue, postcritical ones in red, and the critical (saddle-point) profile in black. Based on the structure of these profiles, we evaluate the quantity $(\partial\rho/\partial r)^2 = \rho'(r)^2$, normalised by its L_2 norm, $||\rho'(r)||_{L_2}$. This normalised profile offers insight into the interfacial region and, in the sharp interface limit, serves as an indicator of the interface location. Specifically, as
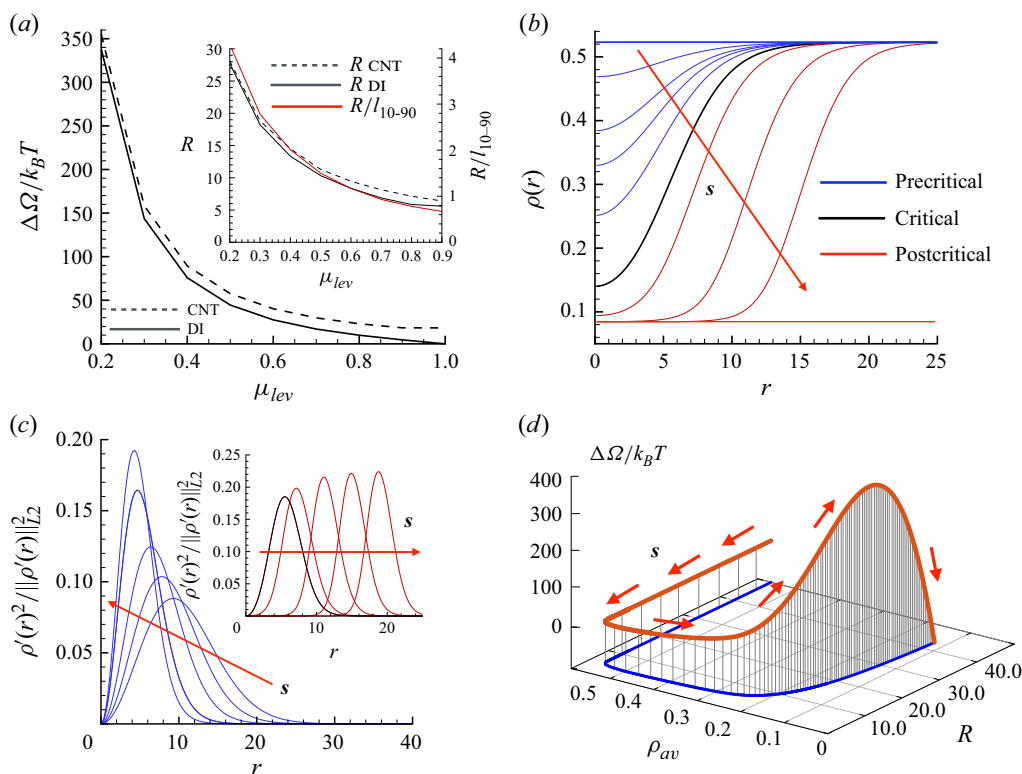
Figure 2. (*a*) Normalised free-energy barrier $\Delta\Omega^\star/k_BT$ versus μ_{lev}. Dashed lines refer to CNT, while solid lines refer to the DI. Inset: the left-hand axis reports R versus μ_{lev}, the right-hand axis depicts R normalised with interface thickness l_{10-90} versus μ_{lev}. (*b*) Density profiles along the transitions, precritical and postcritical profiles are depicted in blue and red, respectively. The critical profile is reported in black ($\mu_{lev} = 0.8$, $T = 1.20$). (*c*) Here $(\partial\rho/\partial r)^2$ normalised with its L_2 norm versus radial coordinate. The panel refers to precritical states, while the inset refers to postcritical conditions. (*d*) Energy landscape as a function of the tuple (ρ_{av}, R), $\mu_{lev} = 0.2$, $T = 1.20$. All cases refer to homogeneous nucleation, the reaction coordinate s increasing directions are also indicated.

the interface thickness tends to zero, $\rho'^2/||\rho'(r)||_{L_2}^2 \to \delta(r - R)$, converging to the sharp interface limit, where δ denotes the Dirac delta function. Within the DI framework, this provides a generalised representation of the interface. This normalised gradient is reported in figure 2(*c*), where the panel shows precritical profiles and the inset includes postcritical profiles and the saddle point. As indicated by the arrow representing the direction of the transition (increasing s), the initial profiles are broad, with maxima located at larger distances r and only modest density variations (red curves in figure 2*b*), corresponding to a slightly rarefied liquid. As the transition proceeds, the maxima shift towards smaller radii and eventually increase in amplitude near the saddle point and beyond (blue curves in figure 2*b*), consistent with the complex C-shaped transition pathway observed in the (R, ρ_{av}) plane. To better highlight the nucleation mechanism, figure 2(*d*) also reports the free energy landscape as a function of the two variables R and ρ_{av}, with the direction of the reaction coordinate s indicated.

A further comparison with heterogeneous CNT is shown in figure 3(*b*) where the ratio between the energy barriers of the heterogeneous and homogeneous cases, $\Delta\Omega^*_{het}/\Delta\Omega^*_{hom}$, is reported as a function of the contact angle. The CNT again provides a theoretical prediction, with this ratio equal to the purely geometrical function $\Psi(\theta) =$
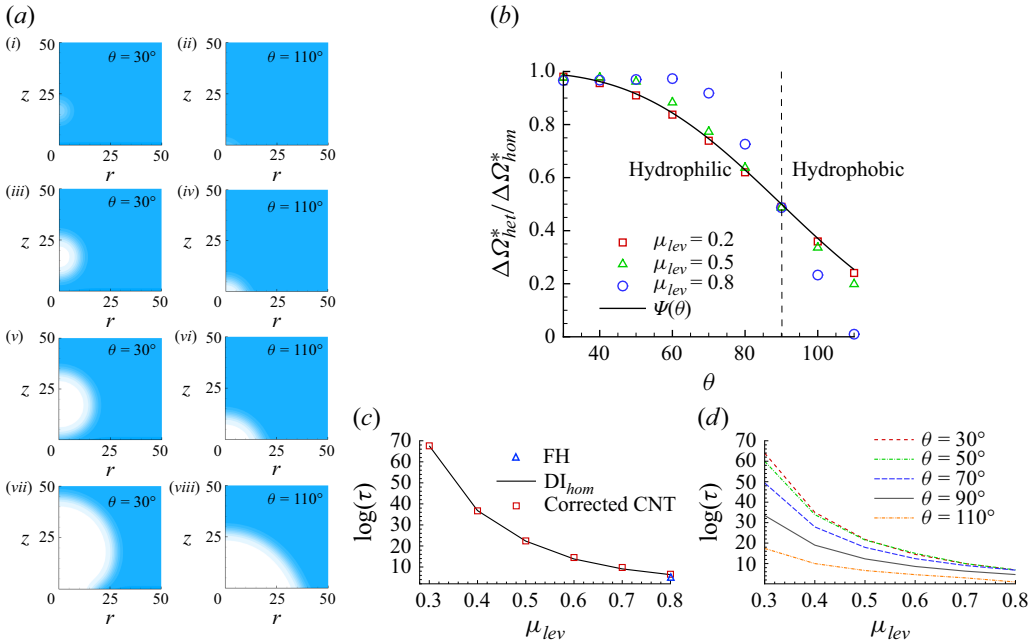
Figure 3. (*a*) Density fields along the MEP, showing nucleation progress from (*i,ii*) to (*vii,viii*). Panels (*a iii*) and (*a iv*) correspond to the transition states: (*iii*) hydrophilic case at $T = 1.2$, $\mu_{lev} = 0.5$, $\theta = 30°$; (*iv*) hydrophobic case at $T = 1.2$, $\mu_{lev} = 0.5$, $\theta = 110°$. (*b*) Energy barrier ratio between heterogeneous and homogeneous nucleation as a function of contact angle, obtained using the string method with the DI model. Symbols indicate different levels of metastability; the solid black curve shows the CNT prediction, based solely on the geometrical factor Ψ. (*c*) Mean first passage time for homogeneous nucleation versus metastability. The solid line is the DI model prediction, while red squares refer to Corrected CNT prediction (Menzl *et al.* 2016), and the blue triangle corresponds to brute force FH simulations. (*d*) The DI model prediction of heterogeneous nucleation's mean first passage time. Each curve corresponds to a different contact angle.

$1/4(2 - \cos(\phi))(1 + \cos(\phi))^2$. The numerical results obtained with the string method applied to the DI model show, instead, a behaviour strongly dependent also on the degree of metastability. Close to saturation, $\mu_{lev} = 0.2$, CNT predictions are well reproduced by the DI model. Mesoscale properties of the critical bubble start to be effective at larger metastability levels. When the interface thickness is comparable to the critical bubble dimension, at $\mu_{lev} = 0.5$ and even more apparently at $\mu_{lev} = 0.8$, the deviation from CNT is more pronounced. It is worth noticing that at high metastability, the hydrophobic surface can anticipate the spinodal condition. The energy barrier at $\mu_{lev} = 0.8$ and $\theta = 110°$ is actually zero, suggesting a barrierless mechanism of phase transition typical of the spinodal decomposition. This result is consistent with the findings of Talanquer & Oxtoby 1996, where the so-called surface spinodal was identified using a different form of fluid–solid free-energy. Moreover, on the hydrophilic side of the plot, the case at $\mu_{lev} = 0.8$ shows a heterogeneous energy barrier independent of the contact angle up to 60° and with a value slightly smaller than the homogeneous barrier. To understand this peculiar behaviour, it is instrumental to look at the full-density fields during the transition progress, shown in figure 3(*a*). The highly hydrophilic surface, even at a moderate metastability level, induces the localisation of the density variation in a region close to the wall but not directly in contact with it. As a consequence, the critical nuclei are almost spherical, resembling homogeneous nucleation. This behaviour has also been observed in full three-dimensional FH simulations (Gallo *et al.* 2021), in MD simulations (Nagayama, Tsuruta &

Cheng 2006; Chen *et al.* 2018; Zou *et al.* 2018) and it could be ascribed to the mesoscale interaction between the vapour–liquid interface and the fluid–solid layering induced by the strong attraction of the hydrophilic surface. The configurations along the MEP show that, after the transition state, the bubble grows at the solid surface, recovering the expected behaviour always observed in experiments. Conversely, in the hydrophobic case, the embryos always sit at the solid wall due to the high affinity with the vapour.

A key observable in stochastic processes such as nucleation is the mean waiting time for forming a critical nucleus. This time scale is usually prohibitively long for direct brute-force simulations (e.g. MD or FH), making theoretical approaches essential. Kramers' theory provides a fundamental framework for estimating the characteristic nucleation rate, see Hänggi *et al.* 1990 for a general discussion on barrier-crossing problems and Gallo *et al.* 2020 for bubble nucleation application. The theory requires the free energy profile and the diffusion coefficient of the fluctuating vapour nucleus embedded in the liquid. Having identified the MEP, described through parameterisation with the curvilinear abscissa s, we can conjecture the simplest dynamics for the reaction coordinate to determine the nucleation times. Such dynamics sees the thermodynamic system as a Brownian walker in the energy landscape $\Omega = \Omega(s)$,

$$\frac{\mathrm{d}s}{\mathrm{d}t} = -\alpha \frac{\mathrm{d}\Omega(s)}{\mathrm{d}s} + \sqrt{2D}\eta(t) \tag{2.5}$$

with α a friction coefficient, $D = k_B T \alpha$ the diffusion and $\eta(t)$ a white noise with zero mean and $\langle \eta(t)\eta(q) \rangle = \delta(t - q)$. The friction coefficient is estimated using the following procedure: the critical bubble $\rho_{crit}(\boldsymbol{x}, s^\star)$ is identified and perturbed along the directions of the two stable basins, ρ_V and ρ_L. The perturbed configurations are then allowed to evolve according to the isothermal NSK equations

$$\frac{\partial \rho}{\partial t} + \boldsymbol{\nabla} \cdot (\rho \boldsymbol{v}) = 0, \tag{2.6}$$

$$\frac{\partial \rho \boldsymbol{v}}{\partial t} + \boldsymbol{\nabla} \cdot (\rho \boldsymbol{v} \otimes \boldsymbol{v}) = -\rho \boldsymbol{\nabla} \left(\frac{\delta \Omega}{\delta \rho} \right) + \boldsymbol{\nabla} \cdot \boldsymbol{\Sigma},$$

where ρ is the density, $\boldsymbol{v}$ is the velocity field and $\boldsymbol{\Sigma} = \eta(\boldsymbol{\nabla}\boldsymbol{v} + (\boldsymbol{\nabla}\boldsymbol{v})^T) + (\zeta - 2/3\eta)$ $(\boldsymbol{\nabla} \cdot \boldsymbol{v})I$ is the viscous stress tensor, η, ζ the two viscosity coefficients. We adopt the viscosity expression proposed by Rowley & Painter 1997 to ensure full consistency with the Lennard-Jones properties. By monitoring the energy variation $\delta\Omega$ occurring as the system transitions between two nearby configurations $\rho(\boldsymbol{x}, s^\star)$ and $\rho(\boldsymbol{x}, s^\star \pm \delta s)$, with $\delta s = ||\rho(\boldsymbol{x}, s^\star \pm \delta s) - \rho(\boldsymbol{x}, s^\star)||_{L^2}$ and the time required for this transition δt (as measured in NSK equations), the friction α is determined as $\alpha = -(\delta s/\delta t)/(\delta\Omega/\delta s)$. Specifically, as detailed in Appendix B, the string is a collection of fields $\rho(\boldsymbol{x}, s)$. We aim to estimate the friction coefficient at the saddle point. Starting from the saddle point, defined by the field $\rho_{crit}(\boldsymbol{x}) = \rho(\boldsymbol{x}, s^\star)$, we introduce perturbations in the directions of the basins of the liquid and vapour by considering the configurations just before and after the saddle point, $\rho(\boldsymbol{x}, s^\star \pm \delta s)$. These are then evolved under the NSK equations towards the respective basins of liquid and vapour. By measuring the time taken to reach the subsequent configurations $\rho(\boldsymbol{x}, s^\star \pm 2\delta s)$, we obtain two values of α, namely $\alpha_r = -(\delta s/\delta t_r)/(\delta\Omega_r/\delta s)$ and $\alpha_l = -(\delta s/\delta t_l)/(\delta\Omega_l/\delta s)$, corresponding to the right- and left-hand sides of the saddle point, with $\delta\Omega_r = \Omega(s^\star + 2\delta s) - \Omega(s^\star + \delta s)$ and $\delta\Omega_l = \Omega(s^\star - 2\delta s) - \Omega(s^\star - \delta s)$, and $\delta t_{r/s}$ the time measured from NSK numerical simulations. We then define the effective diffusion coefficient at the saddle as $\alpha^\star = (\alpha_r + \alpha_l)/2$. The parameter α has physical dimensions of energy times density squared per unit time, while s has the dimensions of a density. This is only an estimate, as the MEP does not represent the

MLP of the NSK dynamics, given that the two systems evolve in different spaces and their trajectories are not necessarily close (Grafke & Vanden-Eijnden 2019; Zakine & Vanden-Eijnden 2023). However, numerical results suggest that the forecast is remarkably accurate, as discussed subsequently. The procedure was repeated for both the homogeneous and heterogeneous cases. After estimating the friction coefficient, the mean first passage time τ was evaluated by using Kramers' theory (Kramers 1940; Schulten, Schulten & Szabo 1981),

$$\tau = \int_{B_L} \exp\left(-\frac{\Delta\Omega}{k_B T}\right) ds \int_{B_{SP}} \frac{1}{D(s)} \exp\left(\frac{\Delta\Omega}{k_B T}\right) ds, \tag{2.7}$$

where B_L and B_{SP} are the metastable and saddle-point basins. The two integrals can be evaluated using the classical saddle-point approximation, after noting that the free energy profiles' curvatures ($\Omega''(s)$) are positive and negative in the two basins, respectively. The second integral can be expanded as

$$\int_{B_{SP}} \frac{1}{D(s)} \exp\left(\frac{\Delta\Omega}{k_B T}\right) ds \sim \exp\left(\frac{\Delta\Omega^\star}{k_B T}\right) \int_{-\infty}^{\infty} \exp\left(-\frac{(s-s^\star)^2}{2\nu^2}\right)$$

$$\times \frac{1}{D^\star + D'_\star(s-s^\star) + 1/2 D''_\star(s-s^\star)^2 + \dots} d(s-s^\star), \tag{2.8}$$

with $\nu^2 = k_B T/|\Omega''(s^\star)|$. Our data show that the diffusion coefficient is gently varying in the neighbourhood of the saddle point, leading to the conclusion that, within an order one prefactor,

$$\tau \sim \frac{2\pi}{\alpha(s^\star)\sqrt{\Omega''(0)|\Omega''(s^\star)|}} \exp\left(\frac{\Delta\Omega^\star}{k_B T}\right). \tag{2.9}$$

Here τ is reported for homogeneous and heterogeneous nucleation in figures 3(c) and 3(d), respectively. Figure 3(c) shows the first passage time as a function of the metastability parameter μ_{lev}. The time is non-dimensionalised using $t_r = 2.15 \times 10^{-12}$ s as a reference. The solid black line depicts our prediction, while the red squares represent the mean first passage time evaluated with an adaptation of the nucleation theory proposed by Menzl *et al.*, (Menzl *et al.* 2016) (see below), and the blue triangle depicts the FH brute force simulations. Kramers' theory becomes increasingly accurate in the limit of large energy barriers (Hänggi *et al.* 1990), see Gallo *et al.* 2020, where the agreement with brute-force simulations emerges for energy barriers $\sim 6-7 k_B T$, at a metastability level of roughly $\mu_{lev} = 0.82$, corresponding to a reduced density of $\rho_L = 0.475$ with $T = 1.25$. In the present case, for the highest metastability level considered ($\mu_{lev} = 0.8$), the energy barrier ($\Delta\Omega^\star \sim 10 k_B T$) is well in the range where Kramers' theory is expected to be robust. This conclusion is supported by 200 FH simulations we performed using the equations reported in Appendix B. The resulting mean first passage for all cases is consistently in the range of $\tau \sim 10^6$ ($\tau_{FH} \sim 0.25 \times 10^6$, $\tau_{DI} \sim 1.00 \times 10^6$, $\tau_{cCNT} \sim 3.60 \times 10^6$) confirming the robustness of Kramers' theory even at moderate metastability. Obviously, also in the heterogeneous case, the accuracy of Kramers' theory may deteriorate for low energy barriers. Such regimes represent only a minor portion of the results presented here, which can, however, be directly investigated via brute-force simulations.

The Menzl *et al.*, theory – applied by the authors to the TIP4P/2005 water model – combines MD microscopic information (vapour embryo surface energy) with the stochastic overdamped Rayleigh–Plesset (RP) equation to estimate the diffusion coefficient D. It is worth noting that the procedure proposed by Menzl *et al.*, is completely general. It consists of correcting the CNT barrier height by either taking the surface energy

from MD simulations or by applying a correction using the Tolman length, which is estimated by adjusting the CNT barrier relative to MD results. The diffusion coefficient of the nucleating bubble is estimated via the fluctuation–dissipation theorem applied to an overdamped RP dynamics, requiring that it samples the equilibrium probability distribution function of the radius R, $P(R) \sim \exp(-\Delta\Omega(R)/k_B T)$. The diffusion coefficient is then computed in closed form as $D_R = k_B T/(16\pi\eta R)$. In the present case, which deals with a Lennard-Jones fluid, the DFT barrier automatically incorporates the curvature correction (Blokhuis & Kuipers 2006; Wilhelmsen, Bedeaux & Reguera 2015; Rehner *et al.* 2019; Magaletti *et al.* 2021) while the diffusion coefficient for reaction variable s is estimated using the hydrodynamic equations with the procedure mentioned above. With this approach, we can directly compare the results of the two theories. We found perfect agreement between the two approaches. The theoretical framework developed by Menzl *et al.*, is not directly applicable to heterogeneous nucleation, as the RP equations describe bubble dynamics in an unbounded medium. In contrast, the approach proposed here is more general, as it allows for the determination of the MEP and the estimation of diffusion coefficients under arbitrary conditions. In figure 3(*d*), the heterogeneous case is presented, highlighting how the wall chemistry plays a crucial role in promoting nucleation by significantly reducing the characteristic transition times. It can be observed that when the contact angle is below approximately 50°, the time scales become independent of wettability, approaching the homogeneous limit. This result is consistent with our previous findings of FH for boiling (Gallo *et al.* 2023) and with MD simulations (Zou *et al.* 2018; Sullivan *et al.* 2025) identifying the homogeneous nucleation as the main transition mechanism when hydrophilic chemistries are considered.

As a final analysis, we examine the velocity fields and the dissipation function of the vapour bubble as it evolves from the saddle point towards the two basins, corresponding to the metastable liquid and the stable vapour. To this end, we introduce the total free energy of the system, defined as the sum of the grand potential and the kinetic energy of the fluid

$$
H[\rho, \boldsymbol{v}] = \Omega[\rho] + K[\rho, \boldsymbol{v}] = \int_V f_b(\rho) + \frac{\lambda}{2}|\boldsymbol{\nabla}\rho|^2 + \frac{1}{2}\rho|\boldsymbol{v}|^2 - \mu_{eq}\rho \, \mathrm{d}V + \oint_{\partial V} f_w(\rho) \, \mathrm{d}S \, .
\tag{2.10}
$$

The dissipation reads

$$
\begin{aligned}
\frac{\mathrm{d}H}{\mathrm{d}t} &= \int_V \frac{\delta H}{\delta \boldsymbol{v}} \cdot \frac{\partial \boldsymbol{v}}{\partial t} + \frac{\delta H}{\delta \rho} \frac{\partial \rho}{\partial t} \, \mathrm{d}V = -\int_V \boldsymbol{v} \cdot \left(\rho \boldsymbol{v} \cdot \boldsymbol{\nabla}\boldsymbol{v} + \rho \boldsymbol{\nabla}\left(\frac{\delta\Omega}{\delta\rho}\right) + \boldsymbol{\nabla} \cdot \boldsymbol{\Sigma} \right) \\
&\quad + \left(\left(\frac{\delta\Omega}{\delta\rho}\right) + \frac{1}{2}|\boldsymbol{v}|^2 \right) \boldsymbol{\nabla} \cdot \rho\boldsymbol{v} \\
&= -\int_V 2\eta \, \tilde{\boldsymbol{E}} : \tilde{\boldsymbol{E}} + \frac{1}{3}\zeta(\boldsymbol{\nabla} \cdot \boldsymbol{v})^2 \, \mathrm{d}V - \oint_{\partial V} \left(\left(\frac{\delta\Omega}{\delta\rho}\right) + \frac{1}{2}|\boldsymbol{v}|^2 \right) \rho\boldsymbol{v} \cdot \hat{\boldsymbol{v}}\mathrm{d}S \, ,
\end{aligned}
\tag{2.11}
$$

where (2.6) have been invoked and $\tilde{\boldsymbol{E}}$ is the deviatoric part of the symmetric part of the velocity gradient $\boldsymbol{E} = \mathrm{sym}(\boldsymbol{\nabla} \otimes \boldsymbol{v})$. In the numerical simulations, the system is large enough that the velocity at the boundary is always zero, so the boundary term in the above equation vanishes and $\mathrm{d}H/\mathrm{d}t < 0$. It is worth noting that, if the total chemical potential $\delta\Omega/\delta\rho + 1/2|\boldsymbol{v}|^2$ is set to zero, then H remains monotonically decreasing in time as well. The simulations were performed in a domain of length $L = 3000$ (dimensionless units), which corresponds to approximately one micron in physical length. Since the present analysis is carried out for homogeneous nucleation, we exploit spherical symmetry to solve (2.6) (Abbondanza *et al.* 2023*b*). We adopt the same grid space Δr, temporal integrator and integration time step Δt of stochastic equations
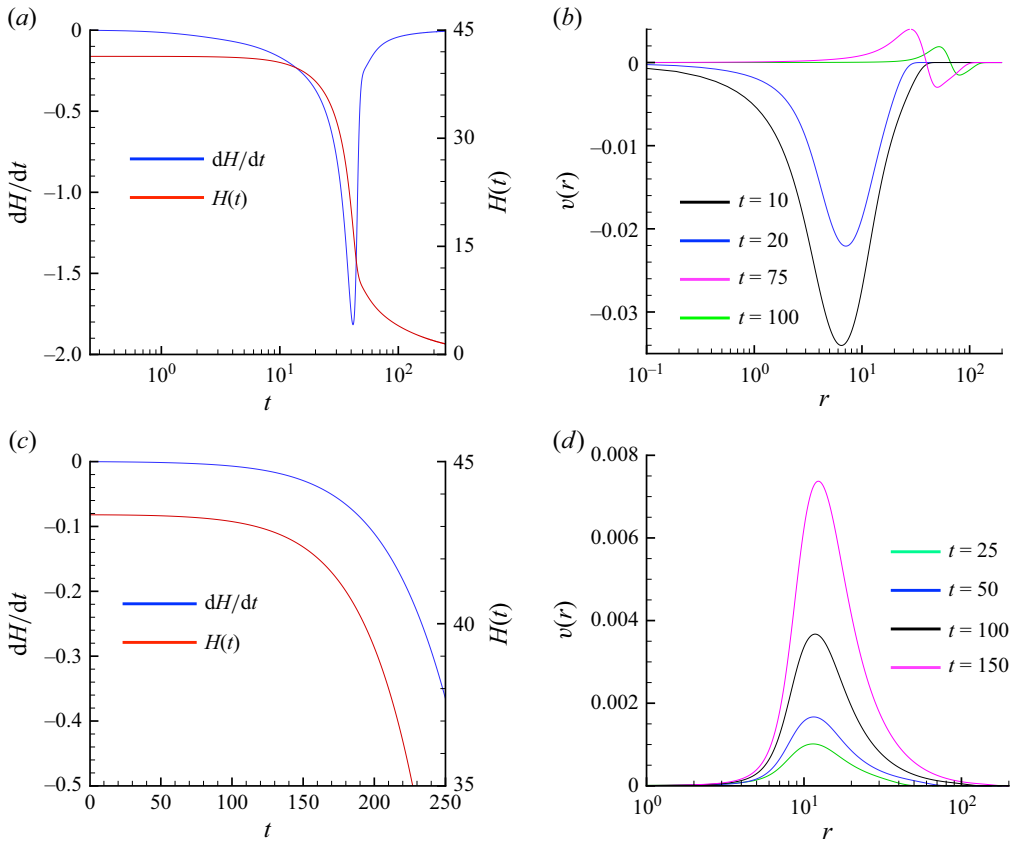
Figure 4. (*a,c*) Time evolution of the dissipation rate $\mathrm{d}H/\mathrm{d}t$ (blue) and total free energy $H(t)$ (red) computed from the NSK dynamics during relaxation towards (*a*) the metastable liquid basin and (*c*) the stable vapour basin. (*b,d*) Velocity profiles at selected time instants during the relaxation towards (*b*) the metastable liquid and (*d*) the stable vapour state.

(see Appendix A for details). The thermodynamic conditions are $T = 1.20$ and $\mu_{lev} = 0.5$. In figure 4, the time evolutions of $H(t)$ (red curves) and $\mathrm{d}H/\mathrm{d}t$ (blue curves) are shown during the hydrodynamic evolution of the bubble in the precritical and postcritical states, in figures 4(*a*) and 4(*c*), respectively. Analogously, figures 4(*b*) and 4(*d*) display the corresponding velocity fields. In both configurations, $H(t)$ decreases monotonically over time, with greater dissipation observed in the precritical phase, characterised by a more abrupt change in the velocity fields. It is particularly interesting to note (figure 4*b*) that the bubble initially shrinks (black curve $t = 10$ and blue curve $t = 20$), then slightly compresses the liquid and emits a wave that propagates through the liquid with the isotermal speed of sound velocity $c_T = \sqrt{\partial p/\partial \rho|_T}$ (purple and green curves at $t = 75$ and $t = 100$). In the postcritical phase, the bubble expands with lower velocities compared with its precritical counterpart.

3. Conclusions

In this work, the MEPs for vapour nanobubble formation in metastable liquids are identified, revealing significant deviations from CNT. Unlike CNT, which assumes a single reaction coordinate (e.g. bubble size), the study shows that nucleation involves both bubble size and average density. Nucleation is triggered by long-wavelength fluctuations

with liquid-like density, forming a C-shaped trajectory in the $\{\rho_{av}, R\}$ space. In both homogeneous and heterogeneous cases, nucleation begins with a large, slightly rarefied cluster that evolves into a stable vapour bubble.

The transition mechanism aligns with FHs simulations, indicating that the MEP closely approximates the MLP under NSK dynamics. Although identifying the MLP remains a complex task, the MEP provides a natural reaction coordinate to construct a simplified stochastic model for estimating transition times. Using NSK dynamics and Kramers' theory, first-passage times are calculated. For the homogeneous case, the predictions match those of Menzl *et al.* 2016 without relying on molecular simulations. In the heterogeneous case, for surfaces with $\phi < 50°$, nucleation follows a homogeneous-like pathway with transition times independent of contact angle – a behaviour inconsistent with CNT but supported by MD and FHs simulations.

A natural extension of this work involves computing the MLP of the FHs via, for example, the minimum action method, which minimises the dynamical action rather than the free energy Weinan, Ren & Vanden-Eijnden (2004). This approach, unlike MEP methods, accounts for non-equilibrium dynamics and full conservation laws (Yao & Ren 2022; Zakine & Vanden-Eijnden 2023; Grafke & Vanden-Eijnden 2019; Soons, Grafke & Dijkstra 2025), and it will be reported elsewhere. An interesting example is the stochastic lubrication theory dynamics in film rupture rare events (Sprittles *et al.* 2023; Liu, Sprittles & Grafke 2024), where the importance of conservation laws shapes rare event kinetics and transition times.

As a final note, we stress that this procedure can be readily extended to real fluids by employing appropriate equations of state, enabling a quantitative prediction of nucleation in realistic systems.

Appendix A: Fluctuating hydrodynamics simulations

The FH equations are Navier–Stokes equations augmented with stochastic fluxes, i.e. the stress tensor and energy flux, to account for thermal fluctuations arising from the discrete nature of matter. These fluxes are derived from a fluctuation–dissipation theorem, ensuring that the equilibrium statistics of the stochastic system sample the Einstein–Boltzmann distribution. The FH offers a powerful framework for quantifying the impact of thermal fluctuations on macroscopic fluid behaviour (Chaudhri *et al.* 2014; Bandak *et al.* 2022; Bell *et al.* 2022; Eyink & Jafari 2022; Barker, Bell & Garcia 2023; Eyink & Jafari 2024; Gallo *et al.* 2023; Gallo & Casciola 2024). In this work, we use our proposed FH extension to multiphase fluids (Gallo *et al.* 2020). This model represents a two-phase liquid–vapour system incorporating thermal fluctuations within the framework of Landau and Lifshitz's FHs. The inclusion of stochastic forcing enables the spontaneous nucleation of vapour clusters within the liquid, while the DI formulation captures the ensuing hydrodynamic processes of growth and transport. Our focus is on a coarse-grained variant of this model, derived by averaging the full three-dimensional equations over spherical shells.

The resulting stochastic equations exhibit a spatial dependence solely on the radial distance from the centre of the vapour cluster. The equations are reported as follows for the readers' convenience:

$$\frac{\partial \rho}{\partial t} = -\frac{1}{r^2}\frac{\partial}{\partial r}\left(r^2 \rho v_r\right), \tag{A1}$$

$$\rho\frac{Dv_r}{Dt} = -\rho\frac{\partial}{\partial r}\left(\frac{\delta \Omega}{\delta \rho}\right) + \frac{1}{r^2}\frac{\partial}{\partial r}\left(r^2 \Sigma_{rr}^v\right) - \frac{2}{r}\Sigma_{\varphi\varphi}^v + \frac{1}{r^2}\frac{\partial}{\partial r}\left(\beta r\, \xi(r,t)\right) + \frac{\beta}{r^2}\xi(r,t), \tag{A2}$$

with

$$\Sigma_{rr}^v = \frac{4}{3}\eta\left(\frac{\partial v_r}{\partial r} - \frac{v_r}{r}\right), \qquad \Sigma_{rr}^v = \frac{2}{3}\eta\left(\frac{v_r}{r} - \frac{\partial v_r}{\partial r}\right) \tag{A3}$$

and

$$\beta = \sqrt{\frac{2k_B T \eta}{3\pi}}, \qquad \langle \xi(r,t)\xi(r',t')\rangle = \delta(r-r')\delta(t-t'). \tag{A4}$$

These equations represent the stochastic extension of (2.6), under the assumption $\zeta = 0$. Numerical simulations have been conducted starting from an initial state with homogeneous (metastable) density and zero velocity. At the boundary, we imposed a fixed density and a vanishing normal derivative of the velocity. Employing the same thermodynamic conditions used for the string computations and a 1000-point grid with dimensionless spacing $\Delta r = 3$. The temporal integrator used is a second-order Runge–Kutta explicit integrator, as it is well-suited for stochastic equations (Delong *et al.* 2013). The (non-dimensional) time step for integration in time was $\Delta t = 10^{-3}$.

Appendix B: The MLP for gradient systems

In this appendix, we aim to elucidate the relationship between the MLP and the MEP for rare trajectories that identify nucleation pathways. These discussions can be found in specialised literature, e.g. in non-equilibrium statistical mechanics of gradient flows (Grafke 2019; Bouchet 2020), or in stochastic process theory (Mielke, Peletier & Renger 2014). Here it is reported in its declination for bubble nucleation. As anticipated in the main text, when the system is subject to a chemical potential within the metastable range, that is

$$\mu_{spin} < \mu_{eq} < \mu_{sat}, \tag{B1}$$

(2.3) admits three distinct steady-state solutions. These correspond to: (i) the uniform liquid phase, characterised by a constant density $\rho(x) = \rho_L$; (ii) the uniform vapour phase, with $\rho(x,t) = \rho_V$; (iii) a non-trivial two-phase configuration in which a vapour nucleus is embedded within a metastable liquid background. This third solution represents a critical state – the so-called critical nucleus – described by the spatially varying density profile $\rho_{crit}(x)$. This configuration acts as a transition threshold: only once the system crosses this critical barrier can it proceed from the metastable liquid to the stable vapour phase, completing the phase transformation. If we assume that the thermodynamic system evolves according to a stochastic gradient dynamics

$$\frac{\partial \rho}{\partial t} = -M\left(\frac{\delta \Omega}{\delta \rho}\right) + \sqrt{2\epsilon}\xi, \tag{B2}$$

with $\epsilon = Mk_B T$ the (small) intensity of the noise, M the mobility and $\xi(x,t)$ a space–time with noise, i.e. $\langle \xi(x,t)\xi(y,q)\rangle = \delta(x-y)\delta(t-q)$. The probability of the phase transition from the liquid state to the vapour one in a certain time window T_w, $P_{\rho_L \to \rho_V}$, is

the probability of observing a given path $\rho(\boldsymbol{x}, t)$ with $-T_w < t < T_w$ with the end states $\rho(\boldsymbol{x}, -T_w) = \rho_L$ and $\rho(\boldsymbol{x}, T_w) = \rho_V$. The large deviation theory provides (Freidlin *et al.* 1998) the probability of observing the path $\rho(\boldsymbol{x}, t)$,

$$P[\rho] \sim \exp\left(-\frac{1}{2\epsilon} S_{T_w}[\rho]\right) , \tag{B3}$$

where

$$S_{T_w}[\rho] = \frac{1}{2} \int_{-T_w}^{T_w} \left\| \frac{\partial \rho}{\partial t} + M\left(\frac{\delta\Omega}{\delta\rho}\right) \right\|^2 dt , \tag{B4}$$

with $\|\cdot\|$ the L_2 norm. Assuming that the trajectory $\rho(\boldsymbol{x}, t)$ crosses the separatrix between the attraction basins of the two minima ρ_L and ρ_V at $t = T_c$, $S_{T_w}[\rho]$ reads

$$S_{T_w}[\rho] = \frac{1}{2} \int_{-T_w}^{T_c} \left\| \frac{\partial \rho}{\partial t} - M\left(\frac{\delta\Omega}{\delta\rho}\right) \right\|^2 dt + \frac{1}{2} \int_{T_c}^{T_w} \left\| \frac{\partial \rho}{\partial t} + M\left(\frac{\delta\Omega}{\delta\rho}\right) \right\|^2 dt$$
$$+ 2M\left(\Omega[\rho(\boldsymbol{x}, T_c)] - \Omega[\rho(\boldsymbol{x}, -T_w)]\right) . \tag{B5}$$

The MLP $\rho^\star(\boldsymbol{x}, t)$ minimises the functional in (B5) in both the window time (T_w) and density space. Concerning time, being ρ_L and ρ_V two minima of the free energy, the minimum of $S_{T_w}[\rho]$ is achieved when $T_w \to \infty$, $S_{T_w}[\rho] \to S_\infty[\rho]$. Therefore, the MLP is given by the two (heteroclinic) orbits

$$\frac{\partial\rho^\star}{\partial t} = M\left(\frac{\delta\Omega}{\delta\rho^\star}\right) \quad \text{for} \quad -\infty < t < T_c , \tag{B6}$$

$$\frac{\partial\rho^\star}{\partial t} = -M\left(\frac{\delta\Omega}{\delta\rho^\star}\right) \quad \text{for} \quad T_c < t < +\infty . \tag{B7}$$

Equation (B7) represents the deterministic dynamics of the spontaneous expansion of the bubble, while (B6) is its time-reversed counterpart. The latter shows that the most likely nucleation event consists of a forward evolution in physical time starting from ρ_L at $t = -\infty$ against the potential gradient up to the saddle point $\rho_{crit}(\boldsymbol{x})$. The MLP $\rho^\star$ has the probability

$$P^\star_{\rho_L \to \rho_V} \sim \exp\left(-\frac{1}{2\epsilon} S_\infty[\rho^\star]\right) = \exp\left(-\frac{\Delta\Omega^\star}{k_B T}\right) , \tag{B8}$$

where $\Delta\Omega^\star = \Omega[\rho_{crit}(\boldsymbol{x})] - \Delta\Omega[\rho_L]$ is the free energy barrier. This result highlights how the nucleation probability and the transition rate exponentially depend on the energy barrier. In principle, one can calculate $\rho^\star$ by looking for the saddle point of $\Delta\Omega[\rho]$, e.g. with the gentlest ascent dynamics (Weinan & Zhou 2011), perturb the dynamics in the directions of maximum descent towards the two stable basins ρ_L and ρ_V and then follow the system's evolution according to (B6) forward in time and the dynamics of (B7) backwards in time, i.e. $t \to -t$. This procedure identifies the MLP with the MEP. The MEP is a continuum sequence of fields $\rho(s, \boldsymbol{x})$ satisfying the condition

$$\left(\frac{\delta\Omega}{\delta\rho}\right)^\perp [\rho(s, \boldsymbol{x})] = 0 , \tag{B9}$$
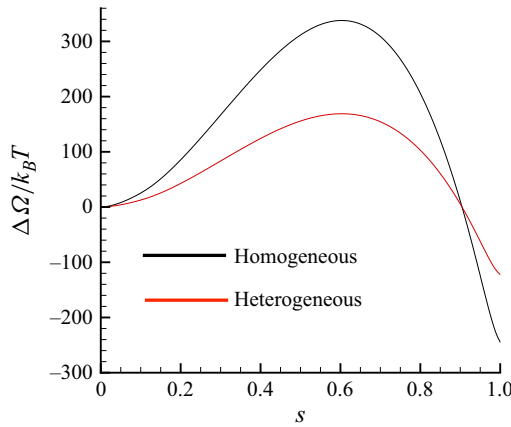
Figure 5. Free-energy profiles as a function of the reaction coordinate s for $T = 1.20$ and $\mu_{lev} = 0.2$. The red and blue curves refer to heterogeneous and homogeneous cases.

with the symbol $\perp$ referring to the projection of the functional derivative onto the space perpendicular to the path

$$\left(\frac{\delta\Omega}{\delta\rho}\right)^{\perp}[\rho(s, \boldsymbol{x})] = \frac{\delta\Omega}{\delta\rho} - \frac{1}{\left\|\dfrac{\partial\rho(\boldsymbol{x}, s)}{\partial s}\right\|^2} \frac{\partial\rho(\boldsymbol{x}, s)}{\partial s} \int_V \frac{\delta\Omega}{\delta\rho} \frac{\partial\rho(\boldsymbol{x}, s)}{\partial s} \, \mathrm{d}V . \tag{B10}$$

The determination of the MEP is achieved by discretising $\rho(s, \boldsymbol{x})$ in a finite number of fields $\rho^s(\boldsymbol{x})$ (images) with $s = 1 \ldots N$. The set of ρ^s forms the string. Starting from a guess string, e.g. linear interpolation between the initial and final states, the sequence is evolved over the pseudotime $\tilde{t}$ according to the steepest descent algorithm

$$\frac{\partial\rho^s}{\partial\tilde{t}} = \mu_{eq} - \mu(\rho^s) + \lambda\nabla^2\rho^s . \tag{B11}$$

To integrate this equation, we employ a staggered spatial scheme: spherical symmetry is used for homogeneous nucleation, while cylindrical symmetry is adopted for heterogeneous cases. Time integration is performed using a forward Euler scheme. After each evolution step over a pseudotime interval $\Delta\tilde{t}$, the images are redistributed along the string through a reparameterisation procedure that enforces equal arclength (E *et al.* 2007), see also Bottacchiari *et al.* 2022, 2024 for application to other DI (Ginzburg–Landau) functionals,

$$\delta s = \left\|\rho^{s+1}(\boldsymbol{x}) - \rho^s(\boldsymbol{x})\right\| = \text{constant} . \tag{B12}$$

This two-step procedure is iterated up to the complete convergence of the whole string to the MEP. Concerning the initial string, we have that $s = 0$ corresponds to the homogeneous metastable liquid, which remains stationary in time. The final condition at $s = 1$ represents the vapour phase at the same chemical potential as the metastable liquid. To accelerate convergence, we initialise the string with a configuration that is qualitatively similar to the formation of a vapour bubble. In particular, the final instance of the initial string is chosen as a large supercritical bubble, with a radius approximately three-quarters of the domain size, which will eventually evolve into a fully developed vapour phase. This choice facilitates the generation of circular, rarefied regions in the liquid. At iteration 0, all intermediate instances are obtained through linear interpolation between the initial and final states. Upon convergence, we obtain the MEP, which we define operationally as

the condition when the energy profile $\Omega(s)$ no longer changes during iterations. For all simulations, the MEP has been discretised using 200 instances along the path. The bubble free energy $(\Omega(s) - \Omega(0))/(k_B T)$ as a function of the reaction coordinate s is shown in figure 5 for both homogeneous and heterogeneous nucleation. The maxima along these profiles correspond to the nucleation energy barriers.

REFERENCES

ABBONDANZA, D., GALLO, M. & CASCIOLA, C.M. 2023*a* Cavitation over solid surfaces: microbubble collapse, shock waves, and elastic response. *Meccanica* **58** (6), 1109–1119.

ABBONDANZA, D., GALLO, M. & CASCIOLA, C.M. 2023*b* Diffuse interface modeling of laser-induced nano-/micro-cavitation bubbles. *Phys. Fluids* **35** (2), 1–8.

ABBONDANZA, D., GALLO, M. & CASCIOLA, C.M. 2024 Collapse of microbubbles over an elastoplastic wall. *J. Fluid Mech.* **999**, A72.

ALAMÉ, K. & MAHESH, K. 2024 Effect of gas content on cavitation nuclei. *J. Fluid Mech.* **982**, A4.

ALLEN, R.J., VALERIANI, C., TEN, W. & REIN, P. 2009 Forward flux sampling for rare event simulations. *J. Phys.: Condens. Matter* **21** (46), 463102.

ANDERSON, D.M., MCFADDEN, G.B. & WHEELER, A.A. 1998 Diffuse-interface methods in fluid mechanics. *Annu. Rev. Fluid Mech.* **30** (1), 139–165.

AZOUZI, M.E.M., RAMBOZ, C., LENAIN, J.-F. & CAUPIN, F. 2013 A coherent picture of water at extreme negative pressure. *Nat. Phys.* **9** (1), 38–41.

BAIDAKOV, V.G. 2016 Spontaneous cavitation in a Lennard–Jones liquid: molecular dynamics simulation and the van der Waals–Cahn–Hilliard gradient theory. *J. Chem. Phys.* **144** (7), 1–11.

BAKIR, M.S. & MEINDL, J.D. 2008 *Integrated Interconnect Technologies for 3D Nanoelectronic Systems*. Artech House.

BANDAK, D., GOLDENFELD, N., MAILYBAEV, A.A. & EYINK, G. 2022 Dissipation-range fluid turbulence and thermal noise. *Phys. Rev. E* **105** (6), 065113.

BARKER, B., BELL, J.B. & GARCIA, A.L. 2023 Fluctuating hydrodynamics and the Rayleigh–Plateau instability. *Proc. Natl Acad. Sci. USA* **120** (30), e2306088120.

BELL, J.B., NONAKA, A., GARCIA, A.L. & EYINK, G. 2022 Thermal fluctuations in the dissipation range of homogeneous isotropic turbulence. *J. Fluid Mech.* **939**, A12.

BLANDER, M. & KATZ, J.L. 1975 Bubble nucleation in liquids. *AIChE J.* **21** (5), 833–848.

BLOKHUIS, E.M. & KUIPERS, J. 2006 Thermodynamic expressions for the tolman length. *J. Chem. Phys.* **124** (7), 1–8.

BOTTACCHIARI, M., GALLO, M., BUSSOLETTI, M. & CASCIOLA, C.M. 2022 Activation energy and force fields during topological transitions of fluid lipid vesicles. *Commun. Phys.* **5** (1), 283.

BOTTACCHIARI, M., GALLO, M., BUSSOLETTI, M. & CASCIOLA, C.M. 2024 The local variation of the Gaussian modulus enables different pathways for fluid lipid vesicle fusion. *Sci. Rep.* **14** (1), 23.

BOUCHET, F. 2020 Is the Boltzmann equation reversible? A large deviation perspective on the irreversibility paradox. *J. Stat. Phys.* **181** (2), 515–550.

CAUPIN, F. 2005 Liquid-vapor interface, cavitation, and the phase diagram of water. *Phys. Rev. E—Stat. Nonlinear Soft Matt. Phys.* **71** (5), 051605.

CAUPIN, F. & HERBERT, E. 2006 Cavitation in water: a review. *C. R. Phys.* **7** (9–10), 1000–1017.

CHAKRABORTY, B., GALLO, M., MARENGO, M., DE CONINCK, J., CASCIOLA, C.M., MICHE, N. & GEORGOULAS, A. 2024 Multi-scale modelling of boiling heat transfer: exploring the applicability of an enhanced volume of fluid method in sub-micron scales. *Intl J. Thermofluids* **22**, 100683.

CHAUDHRI, A., BELL, J.B., GARCIA, A.L. & DONEV, A. 2014 Modeling multiphase flow using fluctuating hydrodynamics. *Phys. Rev. E* **90** (3), 033014.

CHEN, C., GAO, Y., WANG, F. & SUN, C. 2025 A multiscale model for bubble nucleation thresholds on solid walls in the presence of nanometre-sized defects. *J. Fluid Mech.* **1015**, A47.

CHEN, Y., ZOU, Y., WANG, Y., HAN, D. & YU, B. 2018 Bubble nucleation on various surfaces with inhomogeneous interface wettability based on molecular dynamics simulation. *Intl Commun. Heat Mass Transfer* **98**, 135–142.

COCHARD, H. 2006 Cavitation in trees. *C. R. Phys.* **7** (9–10), 1018–1026.

DEBENEDETTI, P.G. 1996 *Metastable Liquids: Concepts and Principles*. Princeton University Press.

DELONG, S., GRIFFITH, B.E., VANDEN-EIJNDEN, E. & DONEV, A. 2013 Temporal integrators for fluctuating hydrodynamics. *Phys. Rev. E* **87** (3), 033302.

DIEMAND, J., ANGÉLIL, R., TANAKA, K.K. & TANAKA, H. 2014 Direct simulations of homogeneous bubble nucleation: agreement with classical nucleation theory and no local hot spots. *Phys. Rev. E* **90** (5), 052407.

DURAN-OLIVENCIA, M.A., YATSYSHIN, P., KALLIADASIS, S. & LUTSKO, J. 2018 General framework for nonclassical nucleation. *New J. Phys.* **35**, (022113-1), 1–18.

E, W., REN, W. & VANDEN-EIJNDEN, E. 2002 String method for the study of rare events. *Phys. Rev. B* **66** (5), 052301.

E, W., REN, W. & VANDEN-EIJNDEN, E. 2007 Simplified and improved string method for computing the minimum energy paths in barrier-crossing events. *J. Chem. Phys.* **126** (16), 164103.

EYINK, G. & JAFARI, A. 2022 High Schmidt-number turbulent advection and giant concentration fluctuations. *Phys. Rev. Res.* **4** (2), 023246.

EYINK, G. & JAFARI, A. 2024 The Kraichnan model and non-equilibrium statistical physics of diffusive mixing. In *Annales Henri Poincaré*, vol. 25, pp. 497–516. Springer.

FAN, S. & DUAN, F. 2020 A review of two-phase submerged boiling in thermal management of electronic cooling. *Intl J. Heat Mass Transfer* **150**, 119324.

FREIDLIN, M.I., WENTZELL, A.D., FREIDLIN, M.I. & WENTZELL, A.D. 1998 *Random Perturbations*. Springer.

FRENKEL, J. 1955 *Kinetic Theory of Liquids*. Dover.

GALLO, M. 2022 Thermal fluctuations in metastable fluids. *Phys. Fluids* **34** (12), 1–11.

GALLO, M. & CASCIOLA, C.M. 2024 Vapor bubble nucleation in flowing liquids. *Intl J. Multiphase Flow* **179**, 104924.

GALLO, M., MAGALETTI, F. & CASCIOLA, C.M. 2018 Fluctuating hydrodynamics as a tool to investigate nucleation of cavitation bubbles. *Multiphase Flow: Theory Applics.* **347**, 345–357.

GALLO, M., MAGALETTI, F. & CASCIOLA, C.M. 2021 Heterogeneous bubble nucleation dynamics. *J. Fluid Mech.* **906**, A20.

GALLO, M., MAGALETTI, F., COCCO, D. & CASCIOLA, C.M. 2020 Nucleation and growth dynamics of vapour bubbles. *J. Fluid Mech.* **883**, 1–29.

GALLO, M., MAGALETTI, F., GEORGOULAS, A., MARENGO, M., DE CONINCK, J. & CASCIOLA, C.M. 2023 A nanoscale view of the origin of boiling and its dynamics. *Nat. Commun.* **14** (1), 6428.

GAO, Z., WU, W. & WANG, B. 2021 The effects of nanoscale nuclei on cavitation. *J. Fluid Mech.* **911**, A20.

GRAFKE, T. 2019 String method for generalized gradient flows: computation of rare events in reversible stochastic processes. *J. Stat. Mech.: Theory Exp.* **2019** (4), 043206.

GRAFKE, T., GRAUER, R. & SCHÄFER, T. 2015 The instanton method and its numerical implementation in fluid mechanics. *J. Phys. A: Math. Theor.* **48** (33), 333001.

GRAFKE, T. & VANDEN-EIJNDEN, E. 2019 Numerical computation of rare events via large deviation theory. *Chaos: Interdiscip. J. Nonlinear Sci.* **29** (6), 1–21.

HÄNGGI, P., TALKNER, P. & BORKOVEC, M. 1990 Reaction-rate theory: fifty years after Kramers. *Rev. Mod. Phys.* **62** (2), 251.

JOHNSON, J.K., ZOLLWEG, J.A. & GUBBINS, K.E. 1993 The Lennard–Jones equation of state revisited. *Mol. Phys.* **78** (3), 591–618.

KRAMERS, H.A. 1940 Brownian motion in a field of force and the diffusion model of chemical reactions. *Physica* **7** (4), 284–304.

LIU, J., SPRITTLES, J.E. & GRAFKE, T. 2024 Mean first passage times and Eyring–Kramers formula for fluctuating hydrodynamics. *J. Stat. Mech.: Theory Exp.* **2024** (10), 103206.

LOHSE, D. & PROSPERETTI, A. 2016 Homogeneous nucleation: patching the way from the macroscopic to the nanoscopic description. *Proc. Natl Acad. Sci. USA* **113** (48), 13549–13550.

LUTSKO, J.F. 2008 Density functional theory of inhomogeneous liquids. III. Liquid–vapor nucleation. *J. Chem. Phys.* **129** (24), 244501.

LUTSKO, J.F. 2011 Density functional theory of inhomogeneous liquids. IV. Squared-gradient approximation and classical nucleation theory. *J. Chem. Phys.* **134** (16), 164501.

LUTSKO, J.F. 2017 Novel paradigms in nonclassical nucleation theory. In *New Perspectives On Mineral Nucleation and Growth: From Solution Precursors to Solid Materials*, pp. 25–41. Springer International Publishing.

LUTSKO, J.F. 2019 How crystals form: a theory of nucleation pathways. *Sci. Adv.* **5** (4), eaav7399.

LUTSKO, J.F. & DURÁN-OLIVENCIA, M.A. 2015 A two-parameter extension of classical nucleation theory. *J. Phys.: Condens. Matter* **27** (23), 235101.

LUTSKO, J.F. & LAM, J. 2020 Long-wavelength density fluctuations as nucleation precursors. *Phys. Rev. E* **101** (5), 052122.

MAGALETTI, F., GALLO, M. & CASCIOLA, C.M. 2021 Water cavitation from ambient to high temperatures. *Sci. Rep.* **11** (1), 20801.

MAGALETTI, F., GALLO, M., PEREZ, S.P., CARRILLO, J.A. & KALLIADASIS, S. 2022 A positivity-preserving scheme for fluctuating hydrodynamics. *J. Comput. Phys.* **463**, 111248.

MENZL, G., GONZALEZ, M.A., GEIGER, P., CAUPIN, F., ABASCAL, J.L.F., VALERIANI, C. & DELLAGO, C. 2016 Molecular mechanism for cavitation in water under tension. *Proc. Natl Acad. Sci. USA* **113** (48), 13582–13587.

MIELKE, A., PELETIER, M.A. & RENGER, D.R.M. 2014 On the relation between gradient flows and the large-deviation principle, with applications to Markov chains and diffusion. *Potential Anal.* **41**, 1293–1327.

MONTAGNA, V.A., PALAGI, S., NASELLI, G.A., FILIPPESCHI, C. & MAZZOLAI, B. 2023 Cavitation-driven deformable microchambers inspired by fast microscale movements of ferns. *Adv. Funct. Mater.* **33** (39), 2214130.

NAGAYAMA, G., TSURUTA, T. & CHENG, P. 2006 Molecular dynamics simulation on bubble formation in a nanochannel. *Intl J. Heat Mass Transfer* **49** (23–24), 4437–4443.

NOBLIN, X., ROJAS, N.O., WESTBROOK, J., LLORENS, C., ARGENTINA, M. & DUMAIS, J. 2012 The fern sporangium: a unique catapult. *Science* **335** (6074), 1322–1322.

OXTOBY, D.W. & EVANS, R. 1988 Nonclassical nucleation theory for the gas–liquid transition. *J. Chem. Phys.* **89** (12), 7521–7530.

REHNER, P., AASEN, A. & WILHELMSEN, Ø. 2019 Tolman lengths and rigidity constants from free-energy functionals—general expressions and comparison of theories. *J. Chem. Phys.* **151** (24), 1–13.

REUTER, F., DEITER, C. & OHL, C.-D. 2022 Cavitation erosion by shockwave self-focusing of a single bubble. *Ultrason. Sonochem.* **90**, 106131.

ROWLEY, R.L. & PAINTER, M.M. 1997 Diffusion and viscosity equations of state for a Lennard–Jones fluid obtained from molecular dynamics simulations. *Intl J. Thermophys.* **18** (5), 1109–1121.

SCHULTEN, K., SCHULTEN, Z. & SZABO, A. 1981 Dynamics of reactions involving diffusive barrier crossing. *J. Chem. Phys.* **74** (8), 4426–4432.

SHEN, V.K. & DEBENEDETTI, P.G. 2001 Density-functional study of homogeneous bubble nucleation in the stretched Lennard-Jones fluid. *J. Chem. Phys.* **114** (9), 4149–4159.

SILBERRAD, D. 1912 Propeller Erosion. *Engineering* **33** (8), 33–35.

SKRIPOV, V.P. 1970 Explosive boiling of liquid and fluctuation nucleus formation. *High Temp.* **8** (4), 782–787.

SOONS, J., GRAFKE, T. & DIJKSTRA, H.A. 2025 Most likely noise-induced tipping of the overturning circulation in a two-dimensional Boussinesq fluid model. *J. Fluid Mech.* **1009**, A53.

SPRITTLES, J.E., LIU, J., LOCKERBY, D.A. & GRAFKE, T. 2023 Rogue nanowaves: a route to film rupture. *Phys. Rev. Fluids* **8** (9), 1–12.

SULLIVAN, P., DOCKAR, D. & PILLAI, R. 2025 Nanoscale surface effects on heterogeneous vapor bubble nucleation. *J. Chem. Phys.* **162** (18), 1–11.

TALANQUER, V. & OXTOBY, D.W. 1996 Nucleation on a solid substrate: a density functional approach. *J. Chem. Phys.* **104** (4), 1483–1492.

THEOFANOUS, T.G., TU, J.P., DINH, A.T. & DINH, T.N. 2002 The boiling crisis phenomenon: Part I: nucleation and nucleate boiling heat transfer. *Expl Therm. Fluid Sci.* **26** (6–7), 775–792.

VERSLUIS, M., SCHMITZ, B., VON DER HEYDT, A. & LOHSE, D. 2000 How snapping shrimp snap: through cavitating bubbles. *Science* **289** (5487), 2114–2117.

VINCENT, O. & MARMOTTANT, P. 2017 On the statics and dynamics of fully confined bubbles. *J. Fluid Mech.* **827**, 194–224.

WEINAN, E., REN, W. & VANDEN-EIJNDEN, E. 2004 Minimum action method for the study of rare events. *Commun. Pure Appl. Maths* **57** (5), 637–656.

WEINAN, E. & ZHOU, X. 2011 The gentlest ascent dynamics. *Nonlinearity* **24** (6), 1831.

WILHELMSEN, Ø., BEDEAUX, D. & REGUERA, D. 2015 Tolman length and rigidity constants of the Lennard-Jones fluid. *J. Chem. Phys.* **142** (6), 1–11.

YAO, W. & REN, W. 2022 Vapor-liquid phase transition in fluctuating hydrodynamics: the most probable transition path and its computation. *J. Comput. Phys.* **467**, 111426.

YATSYSHIN, P. & KALLIADASIS, S. 2021 Surface nanodrops and nanobubbles: a classical density functional theory study. *J. Fluid Mech.* **913**, A45.

ZAKINE, R. & VANDEN-EIJNDEN, E. 2023 Minimum-action method for nonequilibrium phase transitions. *Phys. Rev. X* **13** (4), 041044.

ZHANG, L., 2023 A unifying criterion of the boiling crisis. *Nat. Commun.* **14** (1), 2321.

ZOU, A., GUPTA, M. & MAROO, S.C. 2018 Origin, evolution, and movement of microlayer in pool boiling. *J. Phys. Chem. Lett.* **9** (14), 3863–3869.